Pergamon

Int. J. Solids Structures Vol. 32, No. 8/9, pp. 1063–1077, 1995

0020–7683/95 $9.50 + .00

0020–7683(94)00185–5

EFFECTS OF NONLOCAL DAMAGE IN POROUS PLASTIC SOLIDS

VIGGO TVERGAARD
Department of Solid Mechanics, Technical University of Denmark, DK-2800 Lyngby, Denmark

and

ALAN NEEDLEMAN
Division of Engineering, Brown University, Providence, RI 02912, U.S.A.

(*Received* 26 *May* 1994; *in revised form* 23 *July* 1994)

Abstract—A nonlocal constitutive formulation for a porous ductile material is investigated, in which delocalization relates to the damage mechanism. An elastic–viscoplastic material model is used, with delocalization incorporated in terms of an integral condition on the rate of increase of the void volume fraction. Two model problems are analysed to study the effect of including this material length, one relates to localization of plastic flow in shear bands, while the other considers a metal matrix composite. Both model problems involve final failure in strongly nonhomogeneous strain fields, and it is shown that the inherent mesh sensitivity of the numerical failure predictions can be removed by using the nonlocal material model considered here.

1. INTRODUCTION

Practically all continuum studies of failure in ductile metals have been based on local constitutive relations, which do not represent a material length scale. Unless a length scale is somehow included in the problem formulation, it is well known that numerical predictions of final fracture will show an inherent mesh sensitivity, since the softening material behaviour typical of situations near final failure will tend to give localized damage in regions as narrow as possible within the mesh resolution. For example, studies of ductile crack growth have introduced length scales, by directly specifying the size and spacing of larger voids (Needleman and Tvergaard, 1987, 1991), or the size of cleavage grains in studies accounting also for a brittle failure mechanism (Tvergaard and Needleman, 1993). An investigation of mesh sensitivity in dynamic ductile crack growth showed that the length scale introduced by the spacing of the larger voids could remove the inherent mesh dependence (Needleman and Tvergaard, 1994).

The significance of incorporating a material length scale into constitutive relations has been demonstrated for a number of specific material applications, e.g. for damage development and crack growth in concrete (Bazant *et al.* 1984), or for the modelling of failure by localization in soil or rock (Vardoulakis, 1988). For the case of metals Fleck *et al.* (1993, 1994) have presented experiments that indicate a size effect of the order of a micrometer, and they have argued that this may be explained by geometrically necessary dislocations in the presence of gradients of plastic shear (Ashby, 1970). A variety of constitutive relations for metal plasticity have been proposed that incorporate a material length scale, e.g. Aifantis (1984), Zbib and Aifantis (1989), de Borst (1993), Fleck *et al.* (1993, 1994). But in addition to length scales dependent on plastic deformation mechanisms, there may be other relevant characteristic lengths related to damage development by the nucleation and growth of voids or by microcrack formation. Pijaudier-Cabot and Bazant (1987) and Barenblatt (1992) have suggested nonlocal constitutive formulations in which delocalization relates to the damage mechanism, and the same idea has been used by Leblond *et al.* (1994) in proposing a nonlocal version of the porous ductile material model of Gurson (1977).

In the present paper we use the ideas of Leblond *et al.* (1994) in a study based on an elastic–viscoplastic version of the Gurson model (Pan *et al.*, 1983). Delocalization is incorporated into the constitutive relation in terms of an integral condition on the rate of increase of the void volume fraction, where the characteristic material length may be considered representative of the average void spacing in the material. Leblond *et al.* (1994) have used the corresponding time–independent constitutive relation in a numerical study with very high initial void volume fractions to show that the width of shear bands emanating from an initial imperfection in a plane strain tensile test specimen are indeed controlled by the incorporated length scale. Here, for the viscoplastic material we analyse two model problems, under quasi-static loading conditions, to gain insight into the effect of the delocalization. One problem relates to localization of plastic flow in shear bands, for which a parametric study is carried out, comparing different mesh refinements and different values of the characteristic material length. The other model problem considers metal matrix composites, for which intensive plastic shearing at sharp edges on the ends of brittle fibres tend to show a significant mesh sensitivity in numerical studies based on a local constitutive relation.

2. MATERIAL MODEL

The material model used is based on Gurson's (1975) flow potential for a progressively cavitating solid with a nonlocal evolution equation for the porosity as in Leblond *et al.* (1994). In the present study, the matrix material is taken to be viscoplastic, strain controlled void nucleation is accounted for and the accelerated void growth accompanying coalescence is modelled.

The rate of deformation (the symmetric part of $\dot{\mathbf{F}}\cdot\mathbf{F}^{-1}$, where $\mathbf{F}$ is the deformation gradient), is written as the sum of an elastic part and a plastic part,

$$\mathbf{d} = \mathbf{d}^{\mathrm{e}} + \mathbf{d}^{\mathrm{p}} \tag{1}$$

with

$$\mathbf{d}^{\mathrm{e}} = \mathscr{L}^{-1} : \hat{\boldsymbol{\sigma}}. \tag{2}$$

Here, $\hat{\boldsymbol{\sigma}}$ is the Jaumann rate of Cauchy stress, $\mathbf{A}:\mathbf{B} = A^{ij}B_{ij}$,

$$\mathscr{L} = \frac{E}{1+\nu}\left[\mathbf{I}' + \frac{\nu}{1-2\nu}\mathbf{I}\otimes\mathbf{I}\right] \tag{3}$$

where E is Young's modulus, ν is Poisson's ratio, $\mathbf{I}$ and $\mathbf{I}'$ are the second and fourth order identity tensors, respectively, and $\otimes$ denotes the tensor product, $(\mathbf{A}\otimes\mathbf{B})^{ijkl} = A^{ij}B^{kl}$.

In terms of the void volume fraction, f, and the average strength of the matrix material, $\bar{\sigma}$, the flow potential is

$$\Phi = \frac{\sigma_{\mathrm{e}}^2}{\bar{\sigma}^2} + 2q_1 f^* \cosh\left(\frac{3q_2\sigma_{\mathrm{h}}}{2\bar{\sigma}}\right) - 1 - q_1^2 f^{*2} = 0 \tag{4}$$

with

$$\sigma_{\mathrm{e}}^2 = \tfrac{3}{2}\boldsymbol{\sigma}':\boldsymbol{\sigma}', \quad \sigma_{\mathrm{h}} = \tfrac{1}{3}\boldsymbol{\sigma}:\mathbf{I} \tag{5}$$

and $\boldsymbol{\sigma}' = \boldsymbol{\sigma} - \sigma_{\mathrm{h}}\mathbf{I}$.

The parameters q_1 and q_2 were introduced by Tvergaard (1981, 1982) to bring predictions of the model into closer agreement with full numerical analyses of periodic arrays of voids. The function f^* (f) accounts for the effects of rapid void coalescence at failure and is taken to have the form (Tvergaard and Needleman, 1984),

$$f^* = \begin{cases} f & f \leqslant f_c \\ f_c + \dfrac{f_u^* - f_c}{f_f - f_c}(f - f_c) & f \geqslant f_c \end{cases}. \tag{6}$$

The onset of rapid void coalescence is assumed to begin at a critical void volume fraction, f_c, with f_u^* being the value of f^* at zero stress, i.e. $f_u^* = 1/q_1$. As $f \to f_f$, $f^* \to f_u^*$ and the material loses all stress carrying capacity. Some computations are also carried out using $f^*(f) \equiv f$, in order to separate effects of porosity induced localization from those of failure. The parameter values are taken to be $q_1 = 1.5$ and $q_2 = 1$, and, when eqn (6) is used, $f_f = 0.25$ with f_c either 0.08 or 0.15. Background on this model of a progressively cavitating solid and on the basis for the choice of parameter values is given in Tvergaard (1990a).

With attention restricted to strain controlled nucleation, the local growth of existing voids and the local nucleation of new voids is given by

$$\dot{f}_{\text{local}} = (1-f)\mathbf{d}^p : \mathbf{I} + \mathscr{D}\dot{\bar{\varepsilon}} \tag{7}$$

Void nucleation is taken to follow a normal distribution (Chu and Needleman, 1980) so that

$$\mathscr{D} = \frac{f_N}{s_N\sqrt{2\pi}} \exp\left[-\frac{1}{2}\left(\frac{\bar{\varepsilon} - \varepsilon_N}{s_N}\right)^2\right]. \tag{8}$$

The rate of increase of the void volume fraction in the material point at location $\mathbf{x}$ in the reference configuration is obtained from the local values in eqn (7) by (Leblond *et al.*, 1994; Pijauder-Cabot and Bazant, 1987)

$$\dot{f}(\mathbf{x}) = \frac{1}{W(\mathbf{x})} \int_V \dot{f}_{\text{local}}(\hat{\mathbf{x}}) w(\mathbf{x} - \hat{\mathbf{x}})\, \mathrm{d}\hat{V} \tag{9}$$

where V is the volume of the body in the reference configuration and we use

$$w(\mathbf{z}) = \left[\frac{1}{1 + \left(\dfrac{z}{L}\right)^p}\right]^q \tag{10}$$

with $z = \sqrt{\mathbf{z}\cdot\mathbf{z}}$, a material characteristic length $L > 0$, $p = 8$, $q = 2$ and

$$W(\mathbf{x}) = \int_V w(\mathbf{x} - \hat{\mathbf{x}})\, \mathrm{d}\hat{V}. \tag{11}$$

The local formulation corresponds to the limit $L \to 0$. With $L > 0$, $\dot{f}(\mathbf{x}) \equiv \dot{f}_{\text{local}}$ when $\dot{f}_{\text{local}}$ is spatially uniform. Hence, nonlocality is associated with spatial gradients in $\dot{f}$.

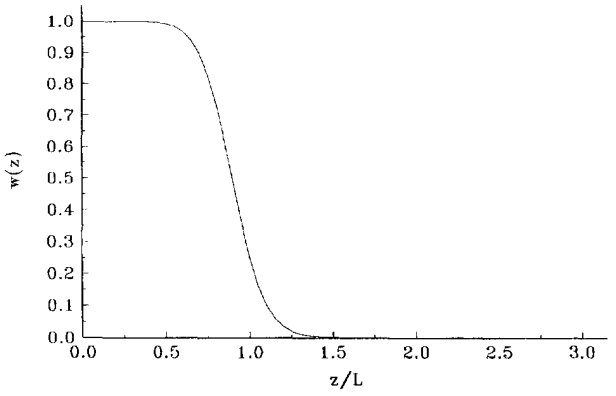

Fig. 1. Delocalization function (10) with $p = 8$ and $q = 2$.

As seen in Fig. 1, the function w is such that $w > 0$ for $z < \mathrm{L}$ and $w \approx 0$ for $z > L$, with a relatively narrow transition region; $w = 0.25$ at $z/L = 1.0$, $w = 0.021$ at $z/L = 1.25$ and $w = 0.0014$ at $z/L = 1.5$. In the computations a cutoff length, $L_c = 1.5L$, is specified such that w in eqn (9) is taken to be zero for $z > L_c$.

At present, there is no micromechanical basis for the nonlocal description. Therefore, choices in the nonlocal modelling have been made arbitrarily or for reasons of computational convenience. For example, the nonlocal transformations for the contributions to $\dot{f}_{\text{local}}$ due to void growth and due to void nucleation in eqn (7) have been assumed to be the same. Also, the integration in eqn (9) is carried out over the reference configuration which reduces the amount of computation, since the influence matrix arising from the discretization of eqn (9) is calculated once and stored. Thus, in the formulation here L is presumably related to the void spacing in the reference configuration.

The matrix material is assumed to be a viscoplastic solid as in Pan *et al.* (1983) and $\mathbf{d}^{\mathrm{p}}$ is obtained from

$$\mathbf{d}^{\mathrm{p}} = \left[\frac{(1-f)\bar{\sigma}\dot{\bar{\varepsilon}}}{\boldsymbol{\sigma}:\dfrac{\partial\Phi}{\partial\boldsymbol{\sigma}}}\right]\frac{\partial\Phi}{\partial\boldsymbol{\sigma}} \tag{12}$$

with the matrix plastic strain rate, $\dot{\bar{\varepsilon}}$, given by

$$\dot{\bar{\varepsilon}} = \dot{\varepsilon}_0\left(\frac{\bar{\sigma}}{g(\bar{\varepsilon})}\right)^{1/m}, \quad g(\bar{\varepsilon}) = \sigma_0[1+\bar{\varepsilon}/\varepsilon_0]^{\mathrm{N}} \tag{13}$$

where $\bar{\varepsilon} = \int \dot{\bar{\varepsilon}}\,\mathrm{d}t$.

Combining (1), (2) and (12) and inverting to obtain the stress rate–strain rate relation gives

$$\hat{\boldsymbol{\sigma}} = \mathscr{L}:\mathbf{d} - \left[\frac{(1-f)\bar{\sigma}\dot{\bar{\varepsilon}}}{\boldsymbol{\sigma}:\dfrac{\partial\Phi}{\partial\boldsymbol{\sigma}}}\right]\mathscr{L}:\frac{\partial\Phi}{\partial\boldsymbol{\sigma}}. \tag{14}$$

3. PROBLEM FORMULATION AND NUMERICAL IMPLEMENTATION

The two model problems to be analysed here are illustrated in Fig. 2. Plane strain conditions are assumed in both cases, and the initial length and width of the unit cells analysed are denoted A_0 and B_0, respectively. The unit cell in Fig. 2(a) represents a material with a doubly periodic array of soft spots, containing initial porosity, as has also been

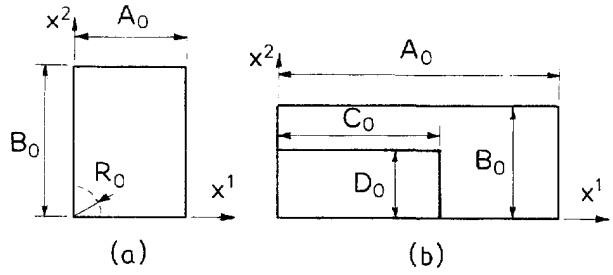

Fig. 2. Two plane strain model problems analysed. (a) Material with doubly periodic array of soft spots. (b) Metal reinforced by short brittle fibres.

studied by Tvergaard (1990b). Figure 2(b) represents a plane strain model of a material with a doubly periodic array of short brittle fibres (as e.g. in Christman *et al.*, 1989). Due to the assumption of plane strain conditions the soft spots and the fibres are in fact cylinders with their axes in the x^3-direction. Hence, the circumstances modelled in Fig. 2(b) can also be regarded as representing the transverse response of a long fibre composite. Symmetry boundary conditions are assumed in the computations

$$\dot{u}^1 = 0, \quad \dot{T}^2 = 0, \quad \text{at } x^1 = 0 \tag{15}$$

$$\dot{u}^2 = 0, \quad \dot{T}^1 = 0, \quad \text{at } x^2 = 0 \tag{16}$$

$$\dot{u}^1 = \dot{U}_\mathrm{I}, \quad \dot{T}^2 = 0, \quad \text{at } x^1 = A_0 \tag{17}$$

$$\dot{u}^2 = \dot{U}_\mathrm{II}, \quad \dot{T}^1 = 0, \quad \text{at } x^2 = B_0 \tag{18}$$

where $\dot{u}^i$ and $\dot{T}^i$ are the displacement components and nominal traction components, respectively, on the reference base vectors. The two constants $\dot{U}_\mathrm{I}$ and $\dot{U}_\mathrm{II}$ are the displacements of the edges, and the ratio $\dot{U}_\mathrm{II}/\dot{U}_\mathrm{I}$ is determined in each increment so that the average overall stress state corresponds to uniaxial plane strain tension.

The initial porosity distribution in the circular soft spot indicated in Fig. 2(a) is specified by

$$f = \Delta f \exp\{-[(x^1)^2 + (x^2)^2]^2/R_0^4\} \tag{19}$$

where Δf is the amplitude and R_0 is the radius. Thus, with the symmetries assumed, the initial spacings between soft spots are $2A_0$ and $2B_0$ in the x^1- and x^2-directions, respectively. In the computations to be shown here, the values $\Delta f = 0.02$ and $R_0/B_0 = 0.08$ are employed. Otherwise the material is taken to be initially void free, but strain controlled nucleation is assumed, with $f_\mathrm{N} = 0.04$, $\varepsilon_\mathrm{N} = 0.3$ and $s_\mathrm{N} = 0.1$ in (8).

In the metal matrix composite, Fig. 2(b), the half fibre length and width are denoted C_0 and D_0, respectively. Generally, brittle fibres have significantly higher elastic modulus than the metal matrix, and here the fibres are approximated as rigid. Thus, with perfect bonding, the additional boundary conditions for the metal region are

$$\dot{u}^1 = \dot{u}^2 = 0, \quad \text{at } x^1 = C_0, \quad x^2 \leqslant D_0 \tag{20}$$

$$\dot{u}^1 = \dot{u}^2 = 0, \quad \text{at } x^2 = D_0, \quad x^1 \leqslant C_0. \tag{21}$$

In the metal strain controlled nucleation with no initial voids is assumed as also specified for the problem of Fig. 2(a).

A convected coordinate Lagrangian formulation of the field equations is used. For the numerical solution a linear incremental solution procedure is employed, with the equations of equilibrium specified in terms of the incremental version of the principle of virtual work

$$\int_V \tau^{ij}\,\delta\eta_{ij}\,\mathrm{d}V = \int_S T^i\,\delta u^i\,\mathrm{d}S. \tag{22}$$

Here, V and S are the volume and surface, respectively, of the region analysed, in the reference configuration, τ^{ij} are the components of the Kirchhoff stress tensor on the current base vectors, and η_{ij} are the Lagrangian strain tensor components. The meshes used for the analyses consist of quadrilaterals, each built up of four simple constant strain triangular elements. This element configuration is well suited for representing shear band localization, as long as the critical orientation of shear bands is along diagonals or sides of the quadrilaterals (Tvergaard *et al.*, 1981).

With the periodicities employed here it is clear that the integral eqn (9) involves also material points outside the region analysed numerically. Due to the periodicities all stress and strain fields are symmetric about the planes $x^1 = 0$, $x^1 = A_0$, $x^2 = 0$ and $x^2 = B_0$, respectively, as implied by eqns (15–18), and thus the needed values of $\dot{f}_{\text{local}}$ are known directly from values inside the quadrant analysed. This has been used in the present analyses, such that the precalculated influence matrix accounts for values of $\dot{f}_{\text{local}}$ outside the region analysed, determined by symmetries. In all cases studied here the cutoff length L_c is smaller than the smallest dimension, A_0 or B_0, of the unit cell, which means that only values of $\dot{f}_{\text{local}}$ in the eight nearest surrounding quadrants are needed for calculating $\dot{f}$ using (9).

The stress rate–strain rate relation (14) could be used directly in the rate form of the principle of virtual work (22) to obtain an incremental solution to the boundary value problems. Because the matrix material is taken to be viscoplastic such an approach would not be complicated by the nonlocal nature of the constitutive relation. Updating would involve calculating $\dot{f}_{\text{local}}$ from (7) and then obtaining $\dot{f}$ from (9). However, very small time steps would be required for numerical stability. In order to increase the stable time step, the rate tangent formulation of Peirce *et al.* (1984) is used. Computing a tangent modulus is complicated by the nonlocal nature of the constitutive relation. The basis for the computation of a tangent modulus (rate dependent or rate independent) is the consistency relation

$$\frac{\partial \Phi}{\partial \boldsymbol{\sigma}} : \dot{\boldsymbol{\sigma}} + \frac{\partial \Phi}{\partial \bar{\sigma}}\,\dot{\bar{\sigma}} + \frac{\partial \Phi}{\partial f}\,\dot{f} = 0 \tag{23}$$

where $\dot{f}$ is given by (9). In the present calculations, $\dot{f}$ is replaced by $K\dot{f}_{\text{local}}$, where $K = \dot{f}/\dot{f}_{\text{local}}$ from the previous time step. Also, to prevent numerical problems when $\dot{f}_{\text{local}}$ is very small, K is taken to be unity if $\dot{f}_{\text{local}}$ is less than 10^{-10}. With $K\dot{f}_{\text{local}}$ replacing $\dot{f}$ in eqn (23), the computation of the rate tangent modulus and the constitutive updating proceeds as for the corresponding local constitutive relation. The time step sizes need to be small enough so that K at any integration point does not vary substantially from step to step.

4. NUMERICAL RESULTS

Fixed material properties are used in the calculations with $\varepsilon_0 = \sigma_0/E = 0.00333$, $N = 0.1$ and $m = 0.00333$ in (13). Also, Poisson's ratio, ν, is taken to be 0.3 and the applied displacement rate, $\dot{U}_1$ in (17), is specified so that $\dot{\varepsilon}_1/\dot{\varepsilon}_0 = 1$, where $\dot{\varepsilon}_1 = \dot{U}_1/(A_0 + U_1)$.

4.1. *Shear band localization*

Figure 3 shows overall stress–strain curves for a material with a doubly periodic array of soft spots. Results are shown for $A_0/B_0 = 0.48$ using four uniform meshes consisting of from 7×7 through 42×42 quadrilaterals (from 196 triangular elements to 7056 triangular elements). Here, $\varepsilon_1 = \ln(1 + U_1/A_0)$ and σ_1 is the corresponding force per unit current area. In Fig. 3(a), the local form of the porous plastic constitutive relation ($L = 0$) is used, while in Fig. 3(b) $L = 0.1B_0$. In these calculations, $f^* \equiv f$ so that there is no loss of stress carrying capacity. Hence, the stress drops in Fig. 3(a) are a consequence of porosity induced localization and not of material failure. There is reasonably good agreement in Fig. 3(a)

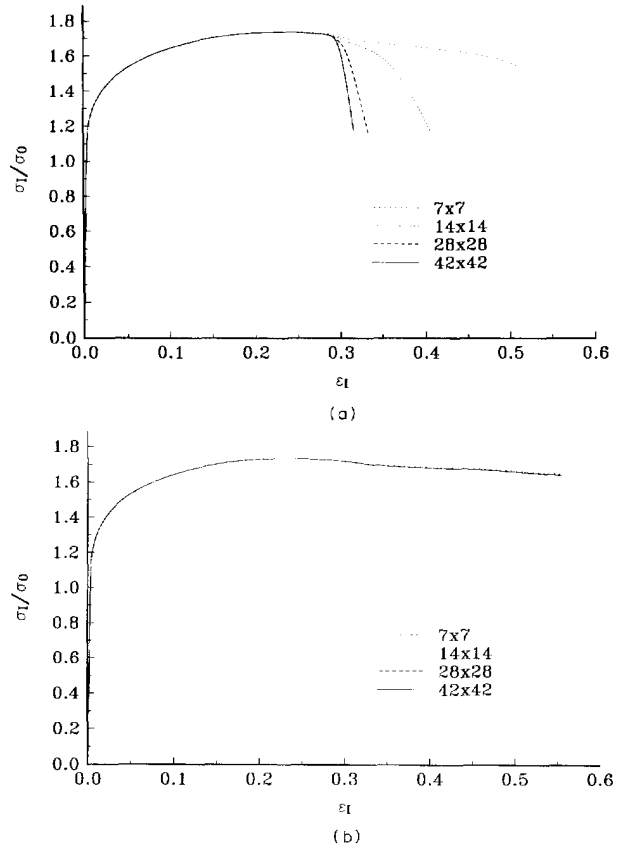

Fig. 3. Overall plane strain stress–strain curves for a material having a doubly periodic array of soft spots, with $A_0/B_0 = 0.48$ and $f^* \equiv f$. (a) $L = 0$. (b) $L = 0.1B_0$.

between the calculations with 14×14, 28×28 and 42×42 quadrilaterals for the value of the overall strain, ε_I, at which the stress drop due to localization begins. However, the post-localization response is clearly very sensitive to the mesh resolution with $L = 0$. In Fig. 3(b), where $L = 0.1B_0$, the overall stress–strain response is essentially identical for all four mesh resolutions and there is no sharp drop in σ_I. With $A_0/B_0 = 0.48$, the quadrilateral diagonals are favorably oriented for shear bands for the local constitutive relation ($L = 0$). For $L = 0.1B_0$ calculations were also carried out using $A_0/B_0 = 0.44$ and $A_0/B_0 = 0.40$ and the overall stress–strain response was found to be insensitive to mesh orientation. Thus, the lack of a stress drop in Fig. 3(b) is not a consequence of the mesh orientation.

It is known from several previous investigations (e.g. see Tvergaard, 1981; Pan *et al.*, 1983) that in plane strain conditions porosity leads to the onset of localization at rather small void volume fractions and that nucleation tends to further enhance the onset of localization. Furthermore, as the regular mesh with crossed triangles can accurately resolve flow localization (Tvergaard *et al.*, 1981; Tvergaard, 1990b), it is known *a priori* for $L = 0$ that localization will be predicted in the cases studied here. The fact that no stress drop is observed in Fig. 3(b) for $L = 0.1\,B_0$ is related to the large influence of shear band width compared to shear band spacing.

Figures 4 and 5 show contours of void volume fraction, f, and deformed quadrilateral meshes for the calculations in Figs 3(a) and 3(b), respectively. What is shown is the deformed configuration of the computational cell; because of the doubly periodic symmetry, the full configuration involves a collection of intersecting shear bands. For each calculation, the stage of deformation shown corresponds to the termination point of the computed overall stress–strain curve. In Fig. 4, where $L = 0$, the shear band width is clearly set by the mesh. On the other hand in Fig. 5, where $L = 0.1B_0$, the shear band width is rather mesh insensitive. There is a significant porosity and deformation gradient across the specimen and the resolution of the gradients increases with increasing mesh refinement. The good

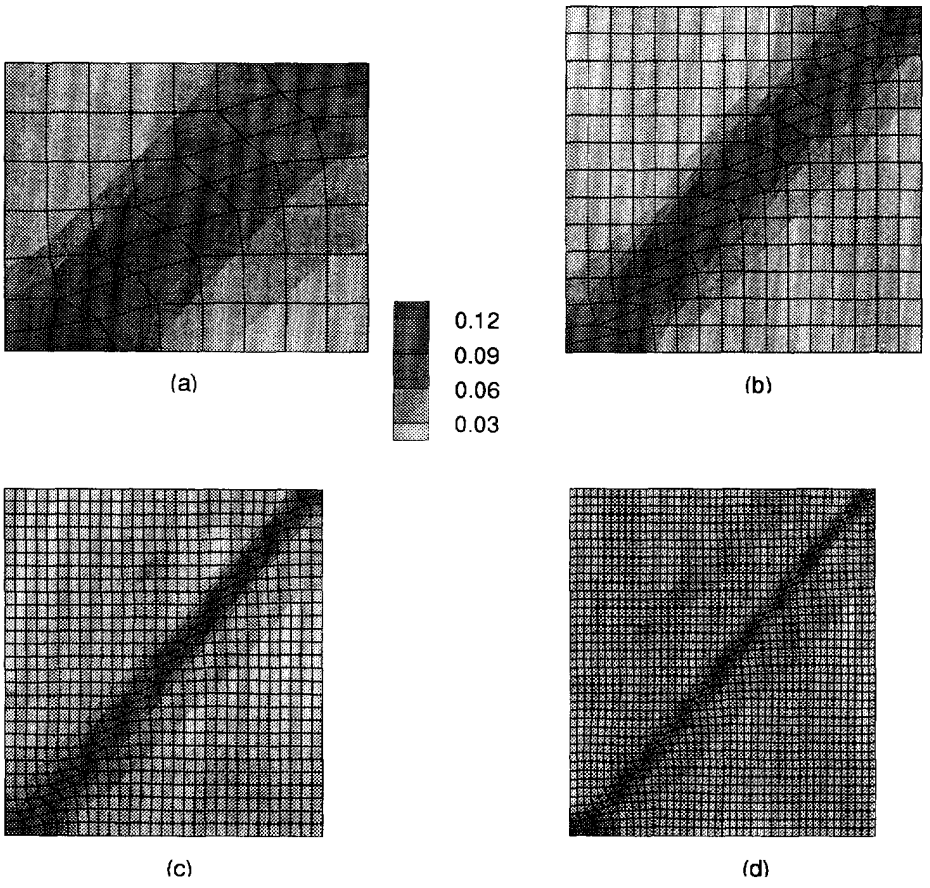

Fig. 4. Contours of void volume fraction, f, for $L = 0$. (a) 7×7 quadrilateral mesh at $\varepsilon_1 = 0.507$. (b) 14×14 quadrilateral mesh at $\varepsilon_1 = 0.405$. (c) 28×28 quadrilateral mesh at $\varepsilon_1 = 0.334$. (d) 42×42 quadrilateral mesh at $\varepsilon_1 = 0.317$.

agreement between the calculations using the 28×28 and 42×42 quadrilateral meshes is evident in Fig. 5 and shows that for $L = 0.1B_0$ the 28×28 mesh gives a converged solution.

The variations of void volume fraction across the specimen for the various meshes is plotted in Fig. 6. These are taken from the contour plots in Figs 4 and 5.† The strong sensitivity of the band width to the mesh for the local constitutive relation is seen in Fig. 6(a). The peak values in Fig. 6(a) should not be compared, because the data for different meshes pertain to different values of the overall strain. On the other hand, in Fig. 6(b), where the value of ε_1 is the same for each case, the peak values as well as the band width can be compared. Even with $L = 0.1B_0$ the 7×7 mesh is too coarse to resolve the gradients in the band. However, because of the broad band, the 14×14 mesh gives a reasonable representation and the results for the 28×28 and 42×42 quadrilateral meshes nearly coincide.

The variation in stress–strain response with L is shown in Fig. 7 using a 28×28 quadrilateral mesh. The curves for $L = 0$ and $L = 0.1B_0$ are repeated from Fig. 3. Corresponding porosity contour plots and deformed meshes are shown in Fig. 8 for $L = 0$, $L = 0.025B_0$, $L = 0.05B_0$ and $L = 0.1B_0$. In Fig. 8(b), where $L = 0.025B_0$, the width of the large shear region is about three elements wide. With $L = 0.05B_0$, the large shear region involves five or six elements and with $L = 0.1B_0$ around ten elements are involved. The increased width of the band, for a fixed mesh, means more elements to resolve the gradients across the band and increased accuracy. Figure 9 shows the porosity variation across the band taken from the contour plots in Fig. 8, where the peak porosity levels should not be compared, as the corresponding overall strain values differ. With $L = 0.1B_0$ and $L = 0.05B_0$,

† Using the commercial plotting program Tecplot from Amtec Engineering Inc., Bellevue, WA.

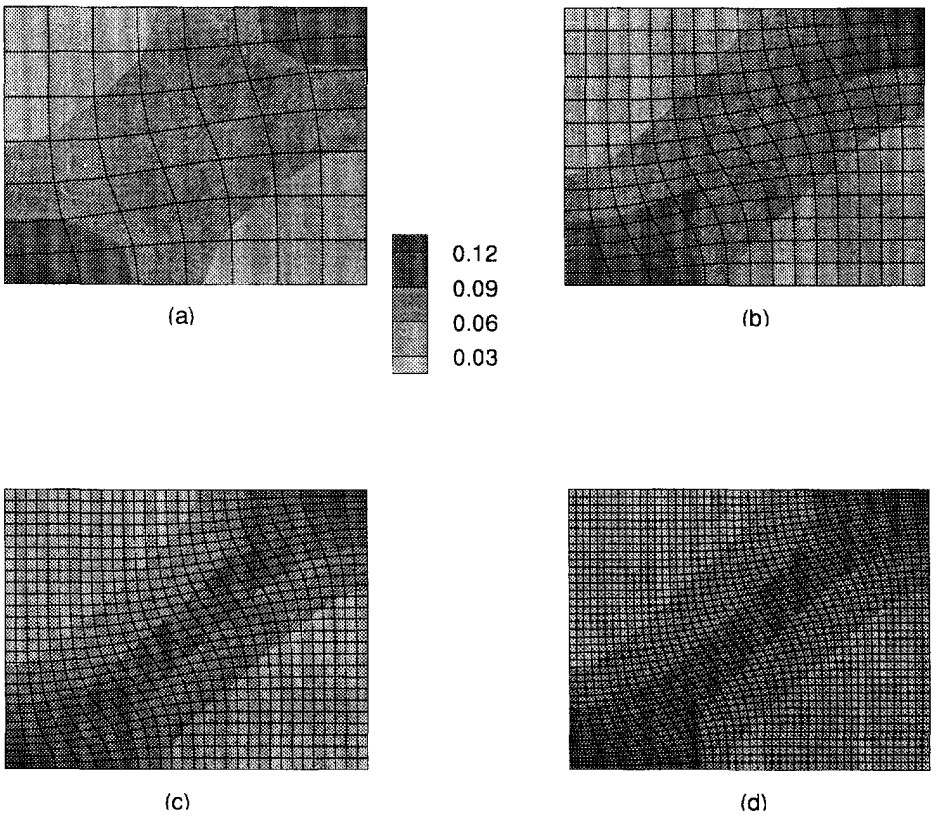

Fig. 5. Contours of void volume fraction, f, for $L = 0.1\,B_0$. (a) 7×7 quadrilateral mesh at $\varepsilon_1 = 0.520$. (b) 14×14 quadrilateral mesh at $\varepsilon_1 = 0.520$. (c) 28×28 quadrilateral mesh at $\varepsilon_1 = 0.520$. (d) 42×42 quadrilateral mesh at $\varepsilon_1 = 0.520$.

the porosity variation is quite smooth, while with $L = 0.025B_0$ the effect of the mesh is evident. For the local constitutive relation, $L = 0$, the band width is set by the mesh.

In the calculations so far, $f^* \equiv f$, so that localization occurs but not material failure, i.e. there is no complete loss of stress carrying capacity. Figure 10 shows results where $f_c = 0.08$ for both $L = 0$ and $L = 0.1B_0$ using 14×14 and 28×28 quadrilateral meshes. The overall stress–strain curves are terminated when a complete loss of stress carrying capacity ($f = f_f$) has taken place in a triangular element. With $L = 0.1B_0$, the overall stress–strain curves are slightly further apart than in Fig. 3(b), where material failure was precluded. This is because of the effect of mesh refinement on resolving the local field concentrations in the inhomogeneity, where failure occurs first. On the other hand, with $L = 0$, the curves for the two mesh resolutions are closer together than in Fig. 3(a). This is because with $f_c = 0.08$ material failure begins before there is much localization. The results in Fig. 10 do show a significant effect of nonlocality on the strain at which failure begins.

4.2. *Failure in metal matrix composites*

The metal–matrix composite calculations are carried out for a 30% reinforcement area fraction, and for a fibre and cell aspect ratio of four, so that $A_0/B_0 = 4$ and $C_0/D_0 = 4$. Figure 11 shows curves of overall stress, σ_1, versus overall strain, ε_1, for four values of L; $L = 1.095D_0$, $L = 0.548D_0$, $L = 0.274D_0$ and $L = 0$. In each case, a mesh consisting of 304 quadrilateral elements (1216 triangular finite elements) was used. Also, in these calculations f_c in eqn (6) is taken to be 0.15. For $L = 0$ and $L = 0.274D_0$, the overall stress–strain curves in Fig. 11 are terminated when material failure has occurred in an element ($f = f_f$). For the calculations with $L = 0.548D_0$ and $L = 1.095D_0$, f exceeds f_c where the porosity is a maximum, but a complete loss of stress carrying capacity has not yet occurred over the strain range shown. Both the maximum stress and the strain at which the maximum stress

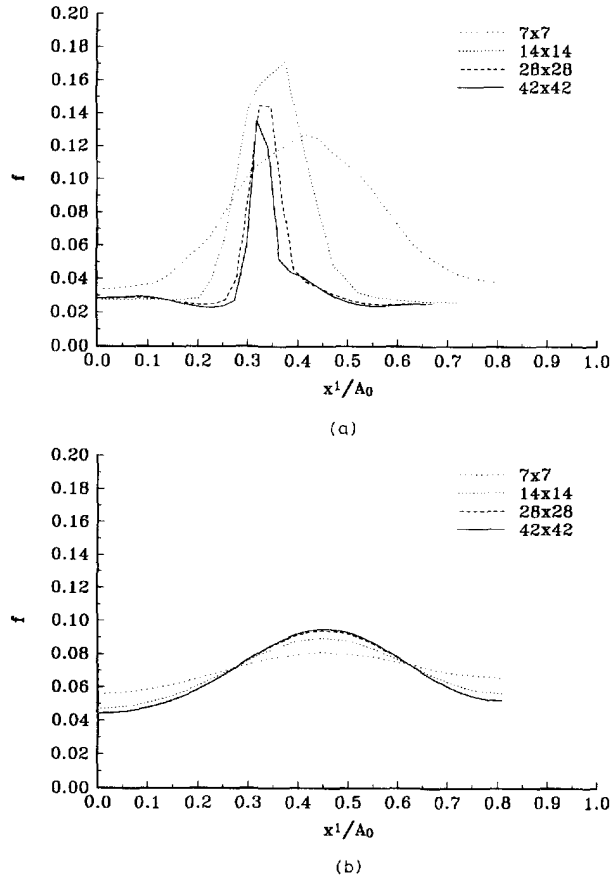

Fig. 6. Curves of void volume fraction, f, versus x^1 at $x^2 \approx 0.35\, B_0$. (a) For $L = 0$ from Fig. 4. (b) For $L = 0.1 B_0$ from Fig. 5.

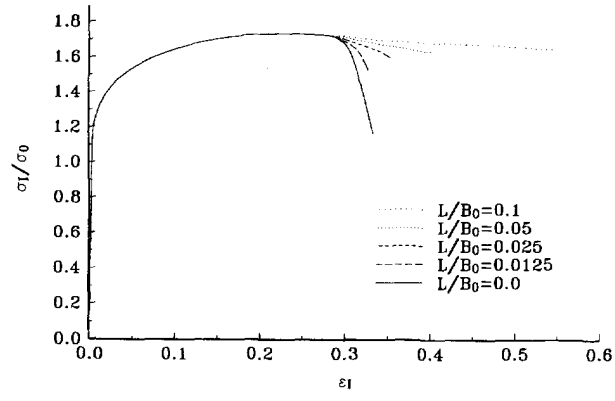

Fig. 7. Variation in overall stress strain response with L using a 28×28 quadrilateral mesh.

occurs increase with increasing L. In addition, the drop in stress carrying capacity is much more gradual for the larger values of L.

Contours of constant void volume fraction, f, and matrix plastic strain, $\bar{\varepsilon}$ are shown in Figs 12 and 13, respectively. In all cases in Fig. 12, the void volume fraction is a maximum along the fibre–matrix interface $x^1 = C_0$. With $L = 0$, this maximum is at the fibre corner ($x^2 = D_0$). With increasing L, the location of the maximum porosity shifts toward the x^1-axis. Additionally, the region of high porosity becomes more spread out with increasing L. The matrix plastic strain contours in Fig. 13 show that the location of the maximum strain remains at the fibre corner for the nonlocal constitutive relation, but the strain concentration there is reduced. The maximum hydrostatic tension, which strongly promotes void growth,

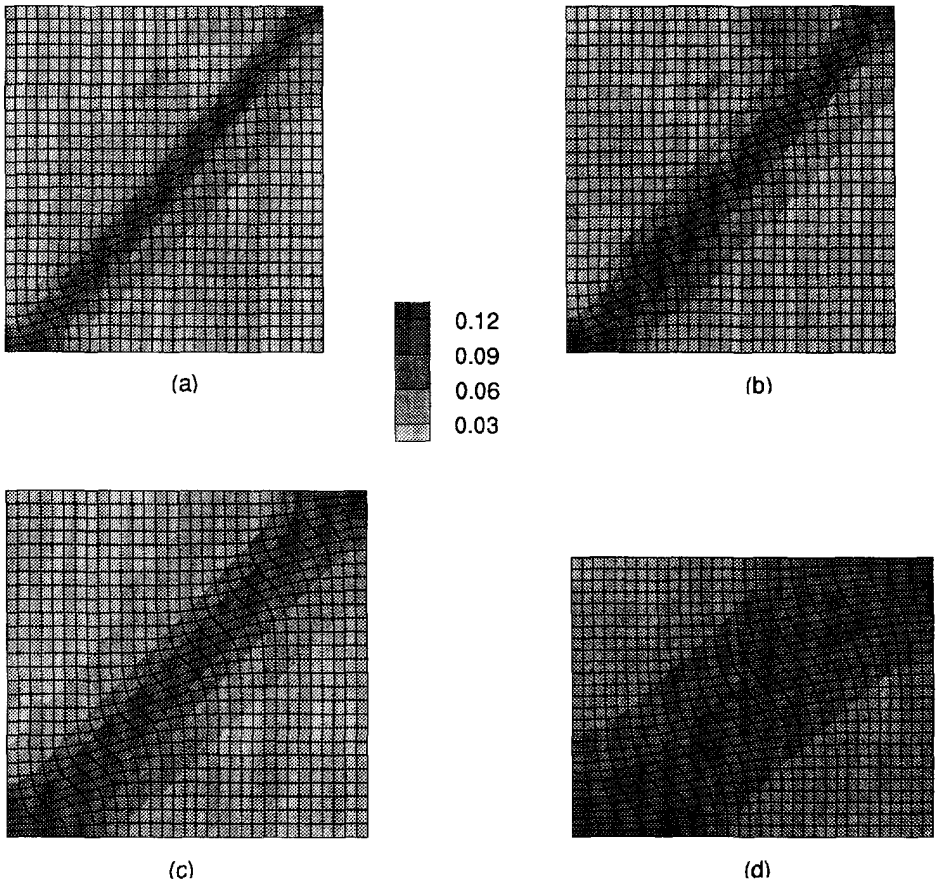

Fig. 8. Contours of void volume fraction, f, for a 28×28 quadrilateral mesh. (a) $L = 0$ at $\varepsilon_1 = 0.334$. (b) $L = 0.025\ B_0$ at $\varepsilon_1 = 0.352$. (c) $L = 0.05\ B_0$ at $\varepsilon_1 = 0.400$. (d) $L = 0.1\ B_0$ at $\varepsilon_1 = 0.520$.

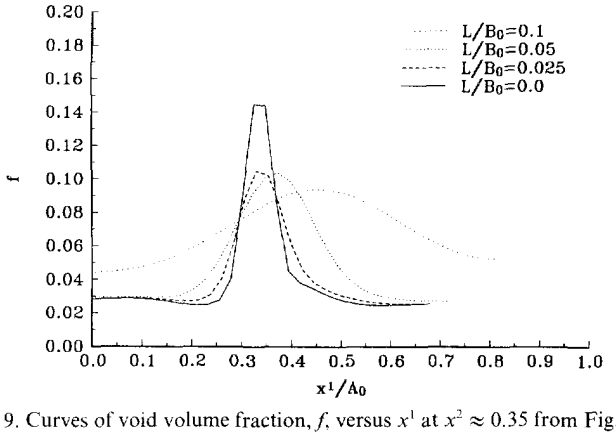

Fig. 9. Curves of void volume fraction, f, versus x^1 at $x^2 \approx 0.35$ from Fig. 8.

occurs near the x^1–axis, while the maximum straining occurs at the fibre corner. For the nonlocal damage relation used here, this shifts the porosity peak from the fibre corner to the fibre center. Additionally, the gradients in both strain and porosity become much less sharp with increasing L. Thus, in this case, nonlocality not only affects when failure occurs but also where failure initiates.

Calculations with $L = 0$ and $L = 1.095D_0$ were also carried out using a mesh with half the number of elements in each direction. In Fig. 14, the coarser mesh consists of 76 quadrilateral elements, while the finer mesh (304 quadrilateral elements) results are taken from Fig. 11. With $L = 0$, the coarse mesh gives rise to a higher load maximum; $3.03\ \sigma_0$ as

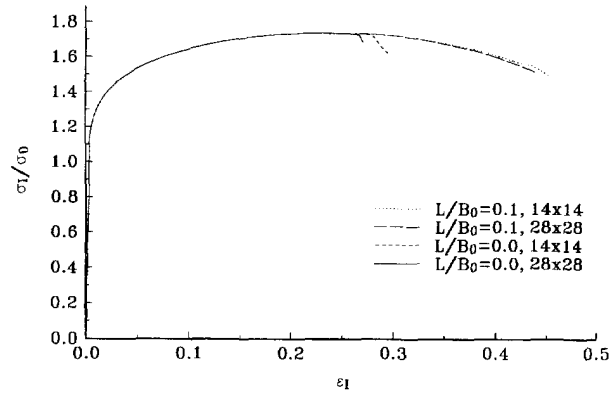

Fig. 10. Overall plane strain stress–strain curves for a material having a doubly periodic array of soft spots, with $A_0/B_0 = 0.48$ and $f_c = 0.08$.

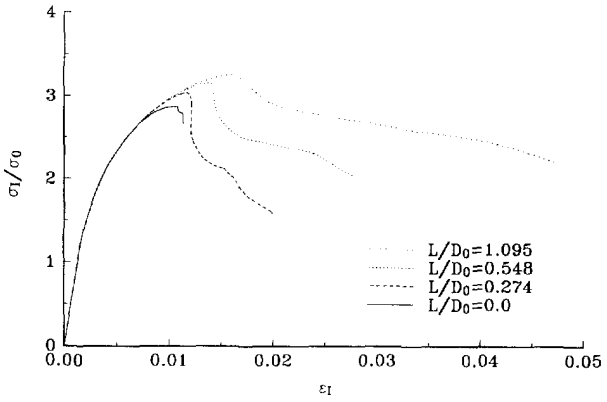

Fig. 11. Overall plane strain stress–strain curves for a material having a doubly periodic array of fibres. The area fraction of fibres is 30%, $A_0/B_0 = 4$ and $C_0/D_0 = 4$.

compared with $2.87\sigma_0$ for the finer mesh and takes place at a slightly larger strain, $\varepsilon_1 = 0.0111$ as compared with $\varepsilon_1 = 0.0104$ for the finer mesh. There is a larger difference between the two meshes for the strain at which a loss of stress carrying capacity first occurs; $\varepsilon_1 = 0.0138$ for the coarse mesh and $\varepsilon_1 = 0.0108$ for the finer mesh used. Thus, for $L = 0$ there is a significant difference in the predictions obtained using these two meshes. On the other hand, with $L = 1.095D_0$, the mesh dependence of the results is much smaller. With the coarse mesh the stress maximum is $3.36\ \sigma_0$ and occurs at $\varepsilon_1 = 0.0157$ whereas with the fine mesh the stress maximum of $3.25\sigma_0$ is at $\varepsilon_1 = 0.0159$. The largest difference between the predictions of the two mesh resolutions occurs before and up to the stress maximum, as is seen in Fig. 14. After the stress maximum, the overall stress–strain curves for the two meshes become closer together and nearly coincide in the range $0.02 \leqslant \varepsilon_1 \leqslant 0.045$. Because the gradients are less severe for larger values of L, once porosity and hence nonlocal effects dominate the stress and deformation distributions, these fields can be resolved with a coarser mesh than needed for the local theory.

5. CONCLUDING REMARKS

A nonlocal elastic–viscoplastic version of the Gurson model, using damage delocalization as proposed by Leblond *et al.* (1994), has been incorporated in a plane strain programme for quasi-static loading conditions. Two model problems are investigated, one involving the onset of localization in shear bands developing towards final void sheet failure, and the other involving metal matrix failure in strongly nonuniform strain fields around brittle fibres.

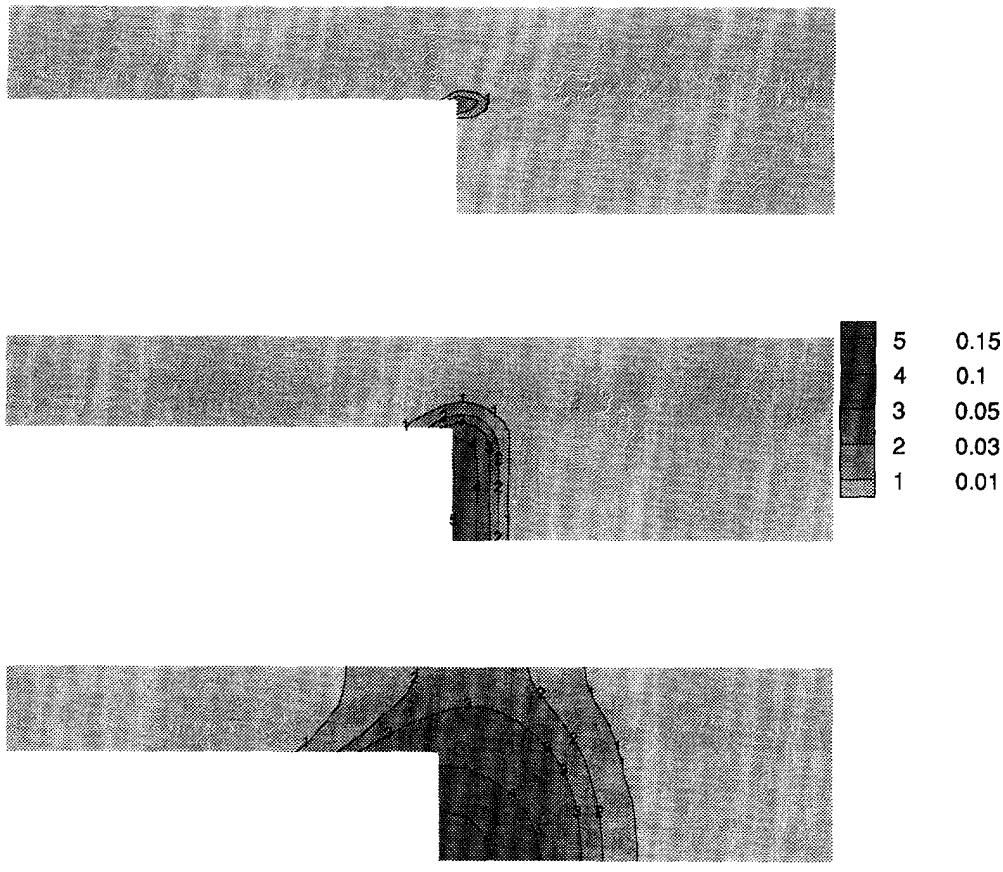

Fig. 12. Contours of void volume fraction, f, for a material having a doubly periodic array of fibres. The area fraction of fibres is 30%, $A_0/B_0 = 4$ and $C_0/D_0 = 4$. (a) $L = 0$ at $\varepsilon_1 = 0.00986$. (b) $L = 0.274D_0$ at $\varepsilon_1 = 0.0163$. (c) $L = 1.095D_0$ at $\varepsilon_1 = 0.0471$.

The main results obtained are the following:

- For shear bands in a local continuum the post-localization behaviour and the subsequent value of the overall strain at final failure are strongly mesh dependent. In the nonlocal continuum, with the characteristic material length specified in terms of an integral condition on the void volume fraction rate, this mesh sensitivity can be completely removed. Thus, for a sufficiently fine mesh relative to the material length, both the shear band width and the peak value of the void volume fraction inside the band are insensitive to the mesh.
- In metal matrix composites, the basic stress and strain fields are very nonuniform, with high peaks at sharp fibre edges. Therefore, in a local continuum early failure will tend to occur at this point. The present results show that both the location where failure initiates and the value of the overall strain at which failure occurs are sensitive to the value of the characteristic material length. This material length, which may be considered representative of the average void spacing in the matrix material, could typically be of the order of magnitude of the fibre diameter. Once failure initiates, results using the nonlocal continuum theory also exhibit much less mesh sensitivity than those for a corresponding local continuum formulation.

Acknowledgments—A. N. is grateful for support provided by the Office of Naval Research through grant N00014-89-J-3054. We are also pleased to acknowledge use of workstations at the Technical University of Denmark and at the Pittsburgh Supercomputer Center.

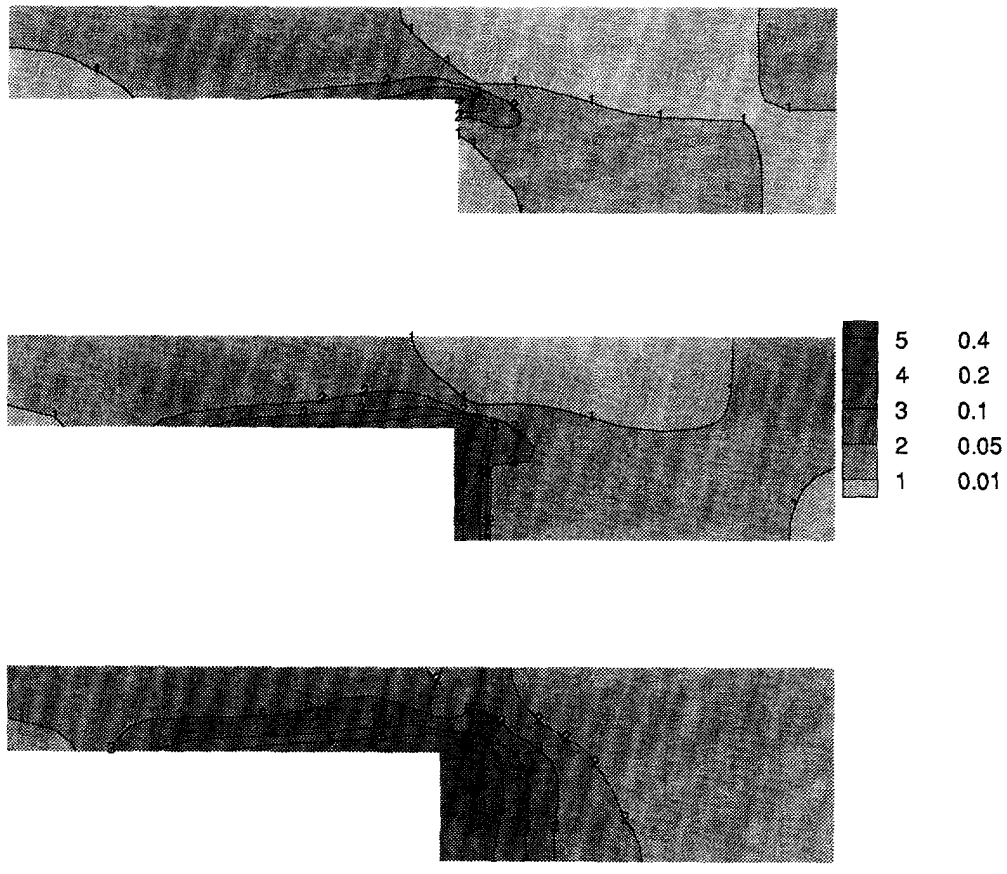

Fig. 13. Contours of matrix plastic strain, $\bar{\varepsilon}$, for a material having a doubly periodic array of fibres. The area fraction of fibres is 30%, $A_0/B_0 = 4$ and $C_0/D_0 = 4$. (a) $L = 0$ at $\varepsilon_1 = 0.00986$. (b) $L = 0.274$ D_0 at $\varepsilon_1 = 0.0163$. (c) $L = 1.095$ D_0 at $\varepsilon_1 = 0.0471$.

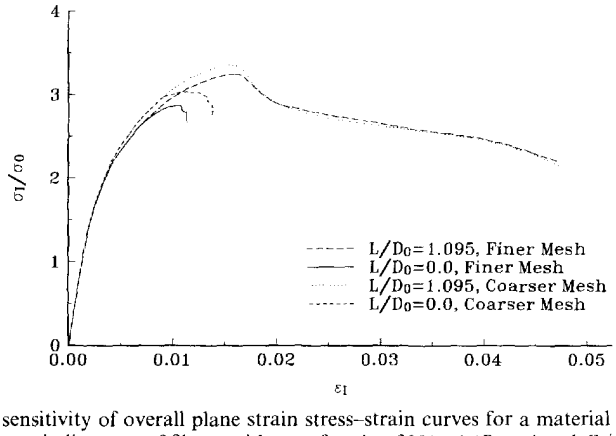

Fig. 14. Mesh sensitivity of overall plane strain stress–strain curves for a material reinforced by a doubly periodic array of fibres, with area fraction 30%, $A_0/B_0 = 4$ and $C_0/D_0 = 4$.

REFERENCES

Aifantis, E. C. (1984). On the microstructural origin of certain inelastic models. *J. Engng Mater. Tech.* **106,** 326–334.

Ashby, M. F. (1970). The deformation of plastically non-homogeneous alloys. *Phil. Mag.* **21,** 399–424.

Barenblatt, G. I. (1992). Micromechanics of fracture. *Proc. Int. Congr. Theor. Appl. Mech.*, Haifa.

Bazant, Z. P., Belytschko, T. B. and Chang, T. P. (1984). Continuum theory for strain softening. *J. Engng Mech. Div. ASCE* **110,** 1666–1692.

de Borst, R. (1993). A generalization of J_2-flow theory for polar continua. *Comput. Meth. Appl. Mech. Engng* **103,** 347–362.

Christman, T., Needleman, A. and Suresh, S. (1989). An experimental and numerical study of deformation in metal–ceramic composites. *Acta Metall.* **37,** 3029–3050.
Chu, C. C. and Needleman, A. (1980). Void nucleation effects in biaxially stretched sheets. *J. Engng Mater. Tech.* **102,** 249–256.
Fleck, N. A. and Hutchinson, J. W. (1993). A phenomenological theory of strain gradient plasticity. *J. Mech. Phys. Solids* **41,** 1825–1857.
Fleck, N. A., Muller, G. M., Ashby, F. and Hutchinson, J. W. (1994). Strain gradient plasticity: theory and experiment. *Acta Metall. Mater.* **42,** 475–487.
Gurson, A. L. (1975). Plastic flow and fracture behavior of ductile materials incorporating void nucleation, growth and interaction. Ph.D. Thesis, Brown University.
Gurson, A. L. (1977). Continuum theory of ductile rupture by void nucleation and growth—I. *Engng Mater. Tech.* **99,** 2–15.
Leblond, J. B., Perrin, G. and Devaux, J. (1994) Bifurcation effects in ductile metals with damage delocalization. *J. Appl. Mech. ASME*, in press.
Needleman, A. and Tvergaard, V. (1987). An analysis of ductile rupture modes at a crack tip. *J. Mech. Phys. Solids* **35,** 151–183.
Needleman, A. and Tvergaard, V. (1991). An analysis of dynamic, ductile crack growth in a double edge cracked specimen. *Int. J. Fracture* **49,** 41–67.
Needleman, A. and Tvergaard, V. (1994). Mesh effects in the analysis of dynamic ductile crack growth. *Engng Fract. Mech.* **47,** 75–91.
Pan, J., Saje, M. and Needleman, A. (1983). Localization of deformation in rate sensitive porous plastic solids. *Int. J. Fracture* **21,** 261–278.
Peirce, D., Shih, C. F. and Needleman, A. (1984). A tangent modulus method for rate dependent solids. *Comput. Struct.* **18,** 875–887.
Pijaudier-Cabot, G. and Bazant, Z. P. (1987). Nonlocal damage theory. *J. Engng Mech. ASCE* **113,** 1512–1533.
Tvergaard, V. (1981). Influence of voids on shear band instabilities under plane strain conditions. *Int. J. Fracture* **17,** 389–407.
Tvergaard, V. (1982). On localization in ductile materials containing spherical voids. *Int. J. Fracture* **18,** 237–252.
Tvergaard, V. (1990a). Material failure by void growth to coalescence. *Adv. appl. Mech.* **27,** 83–151.
Tvergaard, V. (1990b). Effect of anisotropic hardening on ductile failure of a material containing two size-scales of particles. In *Yielding, Damage and Failure of Anisotropic Solids* (Edited by J. P. Boehler), pp. 695–709. Mech. Engng Publ. Ltd, London.
Tvergaard, V. and Needleman, A. (1984). Analysis of the cup–cone fracture in a round tensile bar. *Acta Metall.* **32,** 157–169.
Tvergaard, V. and Needleman, A. (1993). An analysis of the brittle–ductile transition in dynamic crack growth. *Int. J. Fracture* **59,** 53–67.
Tvergaard, V., Needleman, A. and Lo, K. K. (1981). Flow localization in the plane strain tensile test. *J. Mech. Phys. Solids* **29,** 115–142.
Vardoulakis, I. (1988). Theoretical and experimental bounds for shear-band bifurcation strain in biaxial tests on dry sand. *Res. Mechanica* **23,** 239–259.
Zbib, H. M. and Aifantis, E. C. (1989). A gradient-dependent flow theory of plasticity: Application to metal and solid instabilities. *Appl. Mech. Rev.* **42,** S295–S304.